Journal of Membrane Science 666 (2023) 121146

Contents lists available at ScienceDirect

Journal of Membrane Science

journal homepage: www.elsevier.com/locate/memsci

In-situ etching MOF nanoparticles for constructing enhanced interface in hybrid membranes for gas separation

Huiyuan Jiao [a], Yanshu Shi [a], Yapeng Shi [a], Feng Zhang [a], Kuan Lu [c], Yatao Zhang [b], Zhenggong Wang [a,**], Jian Jin [a,*]

[a] *Innovation Center for Chemical Science, College of Chemistry, Chemical Engineering and Materials Science & Collaborative Innovation Center of Suzhou Nano Science and Technology, Soochow University, Suzhou, 215123, China*
[b] *School of Chemical Engineering and Energy, Zhengzhou University, Zhengzhou, 450001, China*
[c] *State Key Laboratory of Coal Conversion, Institute of Coal Chemistry, Chinese Academy of Sciences, Shanxi, 030001, China*

ARTICLE INFO

Keywords:
Hybrid membranes
MOFs nanoparticles
In-situ etching
Interfacial defects
Gas separation

ABSTRACT

Metal-organic frameworks (MOFs) based hybrid membranes have great potential for energy-efficient gas separation. However, the defective interface structure greatly depresses their separation performance. In this work, a distinctive interfacial design strategy *via in-situ* etching ZIF-8 nanoparticles is proposed to construct hybrid membranes with nearly defect-free interfaces. The nanoscale etching of ZIF-8 nanoparticles in polymer matrix with acid group (PI-$COOH_x$) is well controlled by the amount of carboxyl group and reaction time. Owing to the strong coordination interaction between Zn^{2+} ions and –COOH groups, the residual ZIF-8 nanoparticles are tightly wrapped by polymer matrix. Molecular simulation was performed to study the *in-situ* etching ZIF-8 in PI-$COOH_x$ matrix in molecular level. The resulted hybrid membranes (PI-$COOH_x$/E-ZIF-8) exhibit simultaneously enhanced permeability and selectivity with increasing filler loading content. Benefiting from the rational interfacial design, the effective loading content of ZIF-8 nanoparticles is up to 50 wt% for PI-$COOH_{20}$/E-ZIF-8 membrane. The H_2, CO_2, and O_2 permeability of the membrane are 3058.6, 1429.0, and 459.0 Barrer, increasing by 468.5%, 288.3% and 348.2%, respectively, of pristine PI-$COOH_{20}$ membrane, and the gas selectivity for H_2/N_2, H_2/CH_4, O_2/N_2, and CO_2/CH_4 gas pairs are greatly improved from 20.3, 23.4, 3.9 and 16.0 of pristine PI-$COOH_{20}$ membrane to 30.7, 37.6, 4.6 and 17.6. The comprehensive separation performance for H_2/N_2, H_2/CH_4, and O_2/N_2 gas pairs surpass the 2008 upper bound and approach the 2015 upper bound. Meanwhile, the CO_2 plasticization resistance of PI-$COOH_{20}$/E-ZIF-8 membrane also achieves significant improvement from 6 bar of PI-$COOH_{20}$ membrane to 27 bar. This work provides an effective and robust strategy to effectively enhance the interfacial compatibility of hybrid membranes.

1. Introduction

Organic-inorganic hybrid membrane has been regarded as next-generation membrane for gas separation owing to the integration of each advantage [1–3]. Filler phase materials usually play significant roles in enhancing gas separation performance [4]. Among them, microporous materials based molecular sieve including zeolites [5], carbon material [6–9], metal-organic frameworks (MOFs) [10–13], *etc*. Demonstrate remarkably optimized gas sieving property. Metal-organic frameworks (MOFs) are normally constructed from organic ligands and metal ions, possessing high crystallinity, regular pore structure, and high surface areas [14], which make MOFs promising fillers for high-performance hybrid membranes [15–18]. However, most MOFs always possess crystal structure and they are naturally incomparable with amorphous polymers [19,20]. These characteristics have great influence on their efficient loading in polymer matrix especially for some glassy polymers with rigid backbones, resulting in unavoidable interfacial-defects [21].

Interfacial design strategies have been proposed to improve the filler-polymer compatibility of MOF-contained hybrid membranes in recent years. Functionalized MOFs including NH_2-MIL-53 [22], NH_2-UiO-66 [23–25], SO_3H-UiO-66 [26], and COOH-UiO-66 [27] have been

* Corresponding author.
** Corresponding author.
E-mail addresses: zgwang2017@suda.edu.cn (Z. Wang), jjin@suda.edu.cn (J. Jin).

https://doi.org/10.1016/j.memsci.2022.121146
Received 14 August 2022; Received in revised form 26 October 2022; Accepted 31 October 2022
Available online 9 November 2022

synthesized *via* introducing various organic ligands and utilized to enhance interfacial interactions. However, functionalization of MOF is often accompanied by alteration of crystalline structure and difficulty of dispersion in organic solvents. Surface grafting or coating of polymer is another commonly used method to improve the compatibility of MOF fillers in polymer matrix [28–30]. However, some results showed that grafting or coating macromolecule modifier may induce pore blockage [31]. Besides chemical modification mentioned above, regulating and controlling the topological structure of MOFs could be applied to increase surface contacting area and improve interfacial compatibility. Thus, MOF nanosheets as filler material have attracted much attention [32]. Various MOF nanosheets like M-TCPP (M = Zn, Cu, Cd, Co) [33], ZIF-L [34], and ZIF-67 [35] have been incorporated in hybrid membranes. These membranes generally show improved gas permeability and selectivity. Nevertheless, the gas separation performances of these membranes are highly depending on the orientation of nanosheets [36]. To sum up, the current interfacial design strategy usually includes the modification process of MOFs. In this process, the crystallinity, pore structure and dispersion of MOFs are easily broken to varying degrees, thus affecting the performance of hybrid membrane.

It is generally considered that ZIF-8 nanoparticles are easy to be corroded in aqueous solutions, especially in acid condition [37], which is the fatal weakness of this material. However, every coin has two sides [38–40]. The partial decomposition of ZIF-8 nanoparticles could produce a large number of coordinatively unsaturated metal sites along their gradually etched surfaces [41–46]. In this work, we directly take advantage of the *in-situ* etching behavior to construct interfacial defects-free ZIF-8/polymer hybrid membranes with significantly improved gas separation performance. Polyimides functionalized with carboxylic groups (PI-$COOH_x$) are selected as the matrix phase to fabricate the hybrid membranes. In the process of membrane forming, ZIF-8 filler is *in-situ* etched by the carboxylic acid groups and PI-$COOH_x$ interacts with the coordinatively unsaturated metal sites on the surface of etched ZIF-8 to create a nearly defect-free interface (Scheme 1a). By such a design, the gas transportation route across the membrane turns from "bypassing" to "interpenetrating" (Scheme 1b). As a result, the etched ZIF-8 (E-ZIF-8)/polymer hybrid membranes achieve extremely improved gas permeability and selectivity for separating H_2/N_2, H_2/CH_4, and O_2/N_2 gas pairs with comprehensive separation performance surpassing the 2008 Robeson upper bound and approaching the 2015 Robeson upper bound. Moreover, the hybrid membranes demonstrate stable separation performance even under high-pressure mixed gas and possess excellent CO_2 plasticization resistance owing to the enhanced interfacial compatibility.

2. Experimental section

2.1. Materials

4,4'-(hexafluoroisopropylidene) diphthalic dianhydride (6FDA, 99.6%) and 2,3,5,6-teramethyl-1,4-phenylene diamine (Durene, 98%) were purchased from Tokyo Chemical Industrial Co., Ltd. 3,5-diaminobenzoic acid (DABA, 99%), Zinc nitrate hexahydrate ($Zn(NO_3)_2{\cdot}6H_2O$, 99%) and 2-methylimidazole (Hmin, 98%) were purchased from Sigma-Aldrich (Shanghai). Ultra-dry *N*-methyl-2-pyrrolidone (NMP, 99.5%) and N, *N*-dimethylformamide (DMF, 99.5%) were purchased from Alfa Aesar. Methanol (99.5%) and anhydrous toluene (99.5%) were supplied by Sinopham Chemical Reagent Co., Ltd. Ultra-high purity (UHP) grade H_2, N_2, O_2, CH_4, and CO_2 were supplied by Suzhou Jinhong Gas Co., Ltd. Before used, the 6FDA monomer was dried under vacuum at 120 °C for 24 h, and the Durene and DABA monomer were dried under vacuum at 60 °C for 24 h.

2.2. Synthesis of PI-$COOH_x$

PI-$COOH_x$ was synthesized by a polycondensation reaction following

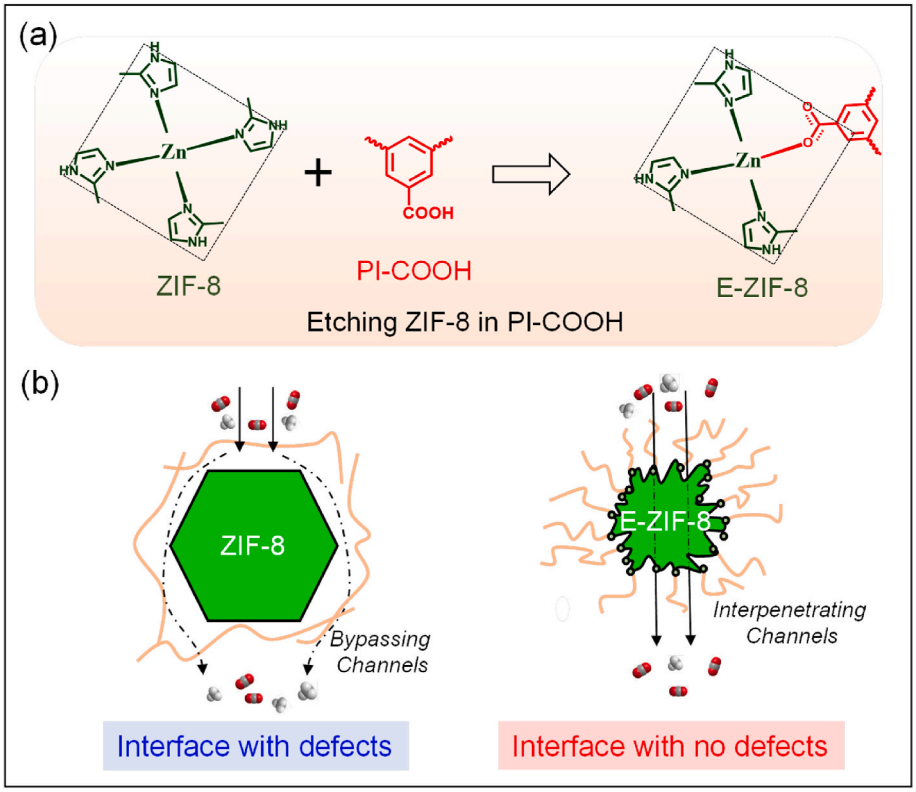

Scheme 1. Schematic illustration of (a) chemical reaction between ZIF-8 and PI-COOH to give rise to the etching of ZIF-8 nanoparticles in PI-COOH matrix and (b) interface structure and gas transportation in ZIF-8 and E-ZIF-8 based hybrid membranes.

our previous study [47–49], where x represents the molar ratios of carboxyl-containing DABA used for synthesis (PI representing the polyimide synthesized without DABA). The molar ratio of Durene and DABA monomers was adjusted accordingly for polyimides with different contents of –COOH groups. The amounts of reagents were summarized (Table S5).

2.3. Synthesis of ZIF-8

Small-size ZIF-8 (~40 nm) was synthesized using a method proposed by previous literature [50]. 2.98 g $Zn(NO_3)_2{\cdot}6H_2O$ (0.01 mol) and 6.56 g 2-methylimidazole (Hmin, 0.08 mol) were dissolved separately in 200 mL methanol. Then the $Zn(NO_3)_2{\cdot}6H_2O$ methanol solution was rapidly poured into 2-methylimidazole methanol solution and stirred for 1 h. The obtained suspension appeared milky white and then centrifuged (8500 rpm, 20 min) at 25 °C and washed by methanol for 3 times to collect the nanoparticles. The obtained ZIF-8 nanoparticles were preserved in methanol for use.

Large-size ZIF-8 (120 nm–155 nm, referred to as L-ZIF-8) nanoparticles were synthesized following the similar procedure [51,52]. 1.52 g 2-methylimidazole (0.018 mol) was dissolved in 10 mL methanol, and then mixed with 0.48 g $Zn(NO_3)_2{\cdot}6H_2O$ (0.0016 mol) dissolved in methanol-water (10 mL: 5 mL) solution. Then the mixture was stirred for 2 h and then centrifuged (8500 rpm, 15 min) at 25 °C and washed by methanol for 3 times.

2.4. Preparation of membranes

The pristine polymer membranes were prepared using the solution casting method. Take the preparation of PI-$COOH_{20}$ membrane as an example. PI-$COOH_{20}$ polyimide was first dissolved in DMF to form a 3–5 wt% solution. Then the solution was stirred for 5 h and stood for 30 min to remove air bubbles. After that, the PI-$COOH_{20}$ solution was filtered through a PTFE filter (Whatman, 0.45 μm) and poured into a leveled PTFE model. The model was put in an oven at 60 °C for 24 h to slowly evaporate the solvent, and then dense membrane was obtained. Then the membranes were dried at 150 °C for 24 h in a vacuum oven to remove any residual solvent. The obtained membranes had a thickness of 100 ± 10 μm. For hybrid membranes preparation, the ZIF-8 methanol solution was first exchanged by DMF. Before used, the ZIF-8 DMF solution was stirred overnight and sonicated for 30 min. Then a certain amount of ZIF-8 solution was added into the PI-$COOH_{20}$ solution, and the mixture was stirred for 30–60 min under 0 °C and stood for 5 min to remove air bubbles. The following procedure was the same as for the

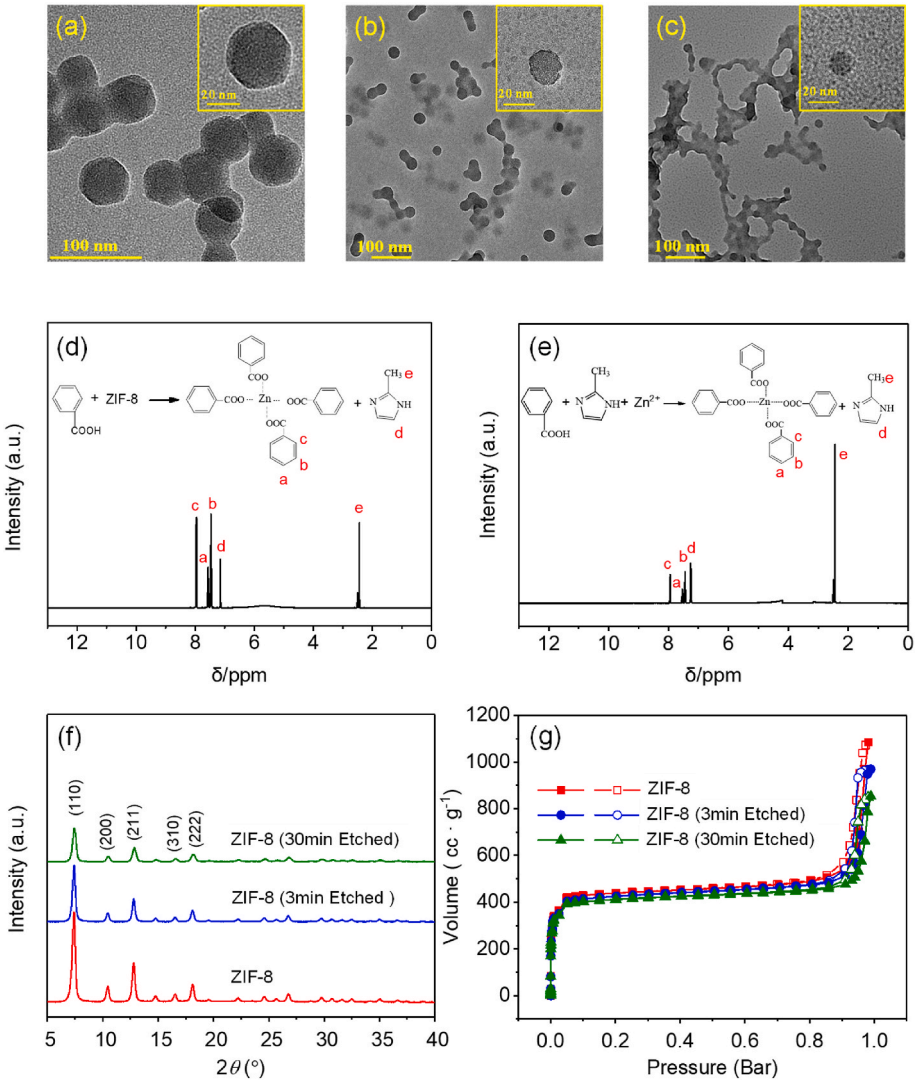

Fig. 1. TEM images of (a) ZIF-8 and ZIF-8 etched by benzoic acid for 3 min (b) and 30 min (c). ^{1}H NMR spectra of (d) the mixture of benzoic acid and ZIF-8 and (e) the mixture of benzoic acid, 2-methylimidazole, and Zn^{2+}. (f) WAXD patterns of ZIF-8, E-ZIF-8 (3 min) and E-ZIF-8 (30 min). (g) N_2 adsorption isotherms at 77 K of ZIF-8, E-ZIF-8 (3 min) and E-ZIF-8 (30 min).

fabrication of PI-$COOH_{20}$ membrane. The obtained hybrid membranes had a thickness of 100 ± 10 μm. And the loading weight was calculated by the following equation (2):

$$\text{ZIF}-8\ \text{loading}\ (\text{wt}\%) = \frac{\text{Weight of ZIF}-8\ (\text{g})}{\text{Weight of ZIF}-8(\text{g}) + \text{Weight of polymer}\ (\text{g})} \quad (1)$$

3. Results and discussion

3.1. Verification of the stability of ZIF-8 nanoparticles in weak acid

The stability of ZIF-8 nanoparticles in weak acid was verified *via* immersing ZIF-8 nanoparticles in benzoic acid solution. The morphology of acid treated ZIF-8 nanoparticles were characterized by transmission electron microscopy (TEM). Fig. 1a–c shows the morphological changes of ZIF-8 nanoparticles treated with acid for 0 min, 3 min and 30 min. The untreated ZIF-8 nanoparticles show rhombic dodecahedron morphology with a particle size of ~40 nm (Fig. 1a). With the acid treatment time increasing to 3 and 30 min, the rectangular outlines of ZIF-8 gradually disappear and their particle sizes decrease to 10–20 nm as shown in Fig. 1b and c, indicating the decomposition of ZIF-8 nanoparticles. The decomposition mechanism was analyzed by examining ^{1}H nuclear magnetic resonance (^{1}H NMR) of the reaction product. The solution for ^{1}H NMR testing was prepared by adding the benzoic acid solution to the milky ZIF-8 dispersion dropwise until the mixture becomes clear and transparent. As a control experiment, a mixture of Zn^{2+}, benzoic acid, and 2-methylimidazole was also prepared. Obviously, the two spectra share same chemical shifts as shown in Fig. 1d and e, indicating that ZIF-8 nanoparticles decompose into 2-methylimidazole and Zn^{2+} in acid condition. The crystal structures of acid treated ZIF-8 were characterized by wide-angle X-ray diffraction (WAXD). Diffraction peaks at 7.3°, 10.4°, 12.8°, 16.5° and 18.1° are observed in the WAXD patterns in Fig. 1f, which corresponds to the crystal planes of (110), (200), (211), (310), and (222), respectively [50]. This indicates the good preservation of crystal structure of ZIF-8 nanoparticles after acid treatment. The peak intensity decreases and the peak width increases with the increasing acid treatment time, indicating the decrease of particle size. The decomposition of ZIF-8 nanoparticles in acid condition was also verified using a large-size ZIF-8 (120–155 nm, L- ZIF-8). Scanning electron microscopy (SEM) images in Fig. S1 show the decrease in particle size and loss of rhombic dodecahedron shape of L-ZIF-8 nanoparticles after acid treatment for 5 min, and 3 h. WAXD patterns in Fig. S2 confirm that the crystal structures of etched L-ZIF-8 nanoparticles are well preserved. Obviously, L-ZIF-8 nanoparticles share similar decomposition behavior with small ZIF-8 nanoparticles in acid condition. The microporous structures of pristine and etched ZIF-8 nanoparticles (~40 nm) were characterized by gas adsorption tests. Fig. 1g shows the N_2 adsorption isotherms (77 K) of ZIF-8 nanoparticles treated with benzoic acid for 0 min, 3 min and 30 min. All the adsorption isotherms belong to typical I-type isotherm with H4-type hysteresis loop, proving the microporous structure of ZIF-8 is well preserved after acid treatment. Thus, the size sieving effect of ZIF-8 nanoparticles would not be comprised after acid treatment. The specific surface area of pristine ZIF-8 and etched ZIF-8 nanoparticles is calculated from the N_2 adsorption isotherms.

By employing the multi-point Brunauer-Emmett-Teller (B.E.T) method. The B.E.T. surface area of pristine ZIF-8 is 1615 $m^2\ g^{-1}$. With the treatment time increasing to 3 and 30 min, the B.E.T surface area increases to 1637 and 1774 $m^2\ g^{-1}$, respectively. Meanwhile, the external surface area of pristine ZIF-8, 3-min-reacted and 30-min-reacted ZIF-8 particles are 118.3 $m^2\ g^{-1}$, 122.3 and 125.9 $m^2\ g^{-1}$, respectively. The slight increase in external surface area is due to the reduction in particle size and increase in surface roughness of ZIF-8 nanoparticles, which is also confirmed by TEM images in Fig. 1. Based on above analysis, it can be deduced that ZIF-8 nanoparticles decompose into 2-methylimidazole and Zn^{2+} in acid condition. Meanwhile, ZIF-8 nanoparticles can maintain the cage structure with reduced particle size and increased specific surface area.

3.2. Fabrication and characterization of PI-COOH/E-ZIF-8 membranes

A carboxylic polyimide (PI–$COOH_{20}$) was selected as matrix phase to mix with ZIF-8 filler to accomplish *in-situ* etching ZIF-8 in polymer matrix. The mixing solution of PI-$COOH_{20}$ and ZIF-8 was stirred under 0 °C for 30–60 min and hybrid membranes were then obtained *via* solution casting method. The *in-situ* etched ZIF-8 inside polymer matrix was named after E-ZIF-8. As a control experiment, hybrid membranes made of polyimide matrix without acid group were also prepared. Fig. 2a exhibits the optical images of PI-$COOH_{20}$/E-ZIF-8 (50 wt%) mixture and PI/ZIF-8 (50 wt%) mixture in DMF. After stirring for 10 h, the mixture of PI-$COOH_{20}$ and ZIF-8 nanoparticles (50 wt%) turns into insoluble gel which is tightly attached to the bottom of bottle, indicating the formation of network structure. In contrast, the mixture of PI and ZIF-8 nanoparticles (50 wt%) remains a homogeneous solution. Solubility tests of PI/ZIF-8 and PI-$COOH_{20}$/E-ZIF-8 membranes with different ZIF-8 loadings were performed by immersing these membranes in DMF solvent for 24 h, as shown in Fig. 2b and c. When the ZIF-8 loading contents increase to 3–10 wt%, the PI-$COOH_{20}$/E-ZIF-8 membranes are partially soluble. With ZIF-8 loading content further increasing to 20 wt% or higher, the PI-$COOH_{20}$/E-ZIF-8 membranes are almost completely insoluble. In contrast, all PI/ZIF-8 membranes are completely dissolved in DMF, and the obtained solutions are milky white just like the ZIF-8 dispersion, indicating the lack of strong interaction between ZIF-8 nanoparticles and PI without –COOH group. The corresponding gel contents are calculated and shown in Fig. 2d. Both pristine PI and PI-$COOH_{20}$ membranes are completely dissolved in DMF. When the ZIF-8 loading increases to 10 wt% and above, PI-$COOH_{20}$/E-ZIF-8 membranes show negligible weight loss (<10%), while the.

PI/ZIF-8 membranes show great weight loss (>70%). The excellent solvent resistance of PI-$COOH_{20}$/E-ZIF-8 membranes is attributed to the formation of strong –COO–Zn^{2+} coordination bond between ZIF-8 nanoparticles and PI-$COOH_{20}$ polyimide.

To study the microstructure of hybrid membranes, WAXD patterns of PI-$COOH_{20}$/E-ZIF-8 and PI/ZIF-8 membranes are measured as shown in Fig. 3a and b. A broad peak at 10°–20° is observed in the patterns of PI-$COOH_{20}$ and PI membranes, indicating their amorphous structures. When the ZIF-8 loading increases to 5–10 wt%, the characteristic peak of ZIF-8 nanocrystal appears in PI/ZIF-8 membranes. However, almost no characteristic peak of ZIF-8 is observed in PI-$COOH_{20}$/E-ZIF-8 membranes, indicating that ZIF-8 nanoparticles have been decomposed by excess carboxylic groups etching. Besides that, the broad peak of PI-$COOH_{20}$/E-ZIF-8 membrane shows slight right shifts with the increasing ZIF-8 loading, indicating that the interchain distance is tightened due to the formation of coordination bonds. When ZIF-8 loading contents reaches to 30–50 wt%, WAXD patterns of both the PI-$COOH_{20}$/E-ZIF-8 and PI/ZIF-8 membranes match well with that of ZIF-8 nanoparticles. This proves that the crystal structure of ZIF-8 nanoparticles can be well preserved even after etched by PI-$COOH_{20}$ polyimide when the ZIF-8 loading is high enough.

The effects of *in-situ* etching ZIF-8 on microstructure of hybrid membranes were also studied by SEM. Fig. 3d, e and 3f show the cross-sectional SEM images of PI-$COOH_{20}$/E-ZIF-8 membranes with 10, 40, and 50 wt% ZIF-8 loading. The ZIF-8 nanoparticles were uniformly dispersed in the PI-$COOH_{20}$ polyimide without agglomeration. The EDX mapping in Fig. S3 demonstrates the uniform distribution of zinc element, further confirming the homogenous distribution of ZIF-8 nanoparticles within PI-$COOH_{20}$/E-ZIF-8 membranes. Almost no voids or interfacial defects could be observed in PI-$COOH_{20}$/E-ZIF-8 membranes even with ZIF-8 loading as high as 50 wt% (Fig. 3f), suggesting the good interfacial compatibility between ZIF-8 nanoparticles and PI-$COOH_{20}$ polyimide. In contrast, all the PI/ZIF-8 membranes show

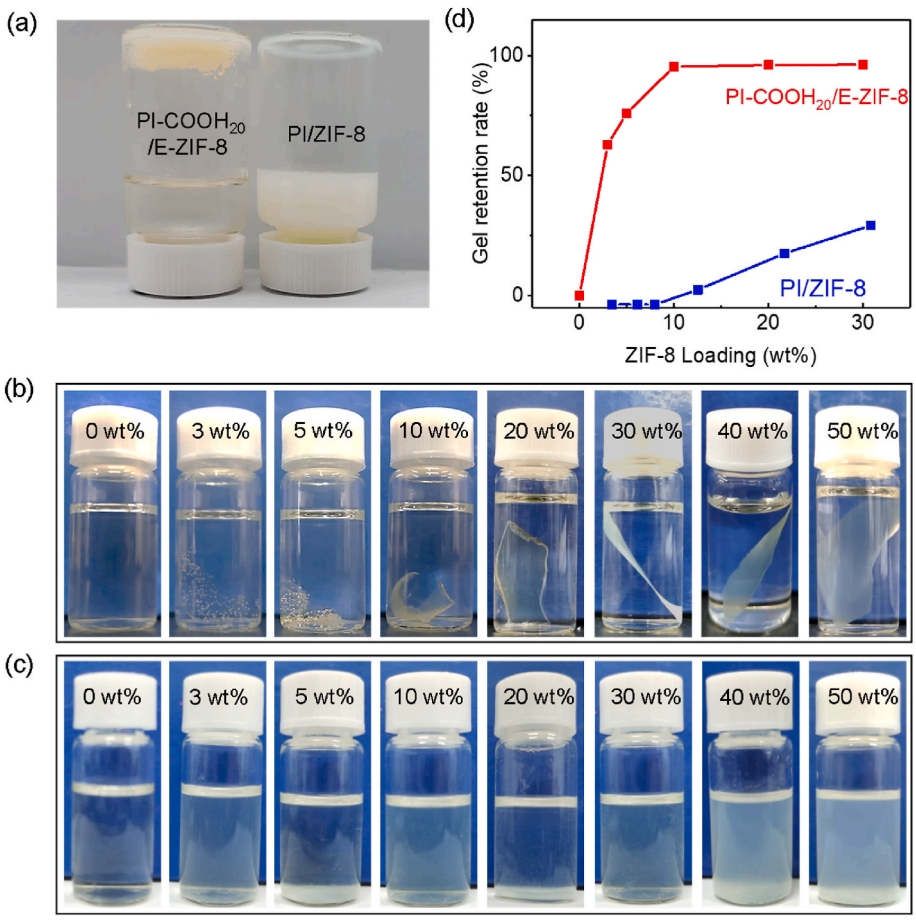

Fig. 2. (a) Optical photos of PI-$COOH_{20}$/E-ZIF-8 (50 wt%) solution and PI/ZIF-8 (50 wt%) solution. (b) Optical photos of PI-$COOH_{20}$ and PI-$COOH_{20}$/E-ZIF-8 (3, 5, 10, 20, 30, 40, and 50 wt%) membranes in DMF. (c) Optical photos of PI and PI/ZIF-8 (3, 5, 10, 20, 30, 40, and 50 wt%) membranes in DMF. (d) Gel contents of PI, PI-$COOH_{20}$, PI/ZIF-8 and PI-$COOH_{20}$/E-ZIF-8 membranes.

obvious phase separation and particle agglomeration, and it becomes more serious with the increasing ZIF-8 loading as shown in Fig. 3g, h and 3i. The reasons for the remarkably different interfacial morphologies are as follows. During the membrane fabrication process, large amounts of coordinatively unsaturated metal sites are generated on the surface of ZIF-8 *via* carboxylic acid etching. Subsequently, the strengthened interface is constructed by the strong coordination bond between E-ZIF-8 nanoparticles and carboxylic polyimide. In contrast, the interfacial interaction of PI/ZIF-8 membrane is only relied on van der Waals forces which are very weak. The optical images of PI-$COOH_{20}$/E-ZIF-8 (50 wt %) and PI/ZIF-8 (50 wt%) membranes are inserted in Fig. 3f and i. Apparently, the PI-$COOH_{20}$/E-ZIF-8 (50 wt%) membrane remains homogeneous and integral, while the PI/ZIF-8 (50 wt%) membrane is fragile and breaks into small pieces, showing the significance of *in-situ* etching ZIF-8 for maintaining good mechanical strength of hybrid membranes. The mechanical strength of PI-$COOH_{20}$, PI, PI-$COOH_{20}$/E-ZIF-8 (30 wt%) and PI/ZIF-8 (30 wt%) membranes were further compared by testing their stress-strain curves (Fig. S4). PI-$COOH_{20}$ and PI membranes show similar mechanical properties with tensile strength of 93.6 MPa and 96.4 MPa, Young's modulus of 2.0 GPa and 2.1 GPa, and break elongation of 9.0% and 7.4%, respectively. After adding filler material, the mechanical strength of two hybrid membranes decreases. However, it should be noted that the tensile strength and Young's modulus of PI-$COOH_{20}$/E-ZIF-8 (30 wt%) membrane are 18.1 MPa and 1.5 GPa much higher than 10.0 MPa and 1.4 GPa of PI/ZIF-8 (30 wt%) membrane. Correspondingly, the break elongation 13.6% of PI-$COOH_{20}$/E-ZIF-8 (30 wt%) membrane is also better than 6.8% of PI/ZIF-8 (30 wt%) membrane. These results confirm that the formation of coordination bond between ZIF-8 nanoparticles and PI-$COOH_{20}$ polyimide can effectively enhance the mechanical strength of hybrid membranes. The thermal stability of ZIF-8 nanoparticles, PI-$COOH_{20}$ membrane, and PI-$COOH_{20}$/E-ZIF-8 membranes was characterized by thermal gravimetric analysis (TGA) under N_2 atmosphere. As shown in Fig. S5, no weight loss is observed at 100–200 °C, indicating the complete removal of residual solvents in PI-$COOH_{20}$/E-ZIF-8 membranes. The thermal decomposition temperature (T_d, 10% mass loss) of PI-$COOH_{20}$ membrane is around 550 °C. Notably, the thermal decomposition temperatures of all PI-$COOH_{20}$/E-ZIF-8 membranes are all around 500 °C, showing negligible effect of ZIF-8 incorporation on the membrane thermal stability.

Attenuated Total Reflection Fourier Transform Infrared (ATR-FTIR) spectra of PI-$COOH_{20}$ and PI-$COOH_{20}$/E-ZIF-8 (40 wt%) membranes were characterized, as shown in Fig. 3c. The two membranes share similar spectra, where the absorption peaks at 1786 and 1721 cm^{-1} are assigned to the C═O of imide bonds, and the absorption peak at 1624 cm^{-1} is assigned to the asymmetric stretching vibration of –COOH. After the incorporation of E-ZIF- 8, the intensity of the absorption peak assigned to –COOH decreases, while a new absorptionpeak at 1583 cm^{-1} appears, which is assigned to asymmetric stretching vibration of –COO–. This is attributed to the coordination interaction between carboxyl and Zn^{2+}. Besides that, an absorption peak at 690 cm^{-1} is observed in the spectrum of PI-$COOH_{20}$/E-ZIF-8 (40 wt%) membrane and assigned to the *N*–Zn^{2+} coordination bond in ZIF-8 nanoparticles, verifying the existence of ZIF-8 nanoparticles in the membrane. Fig. S6 shows the X-ray photoelectron spectra (XPS) of PI-$COOH_{20}$, PI-$COOH_{20}$/E-ZIF-8 (10 wt %) and PI-$COOH_{20}$/E-ZIF-8 (40 wt%) membranes. Besides C 1s, N 1s, O

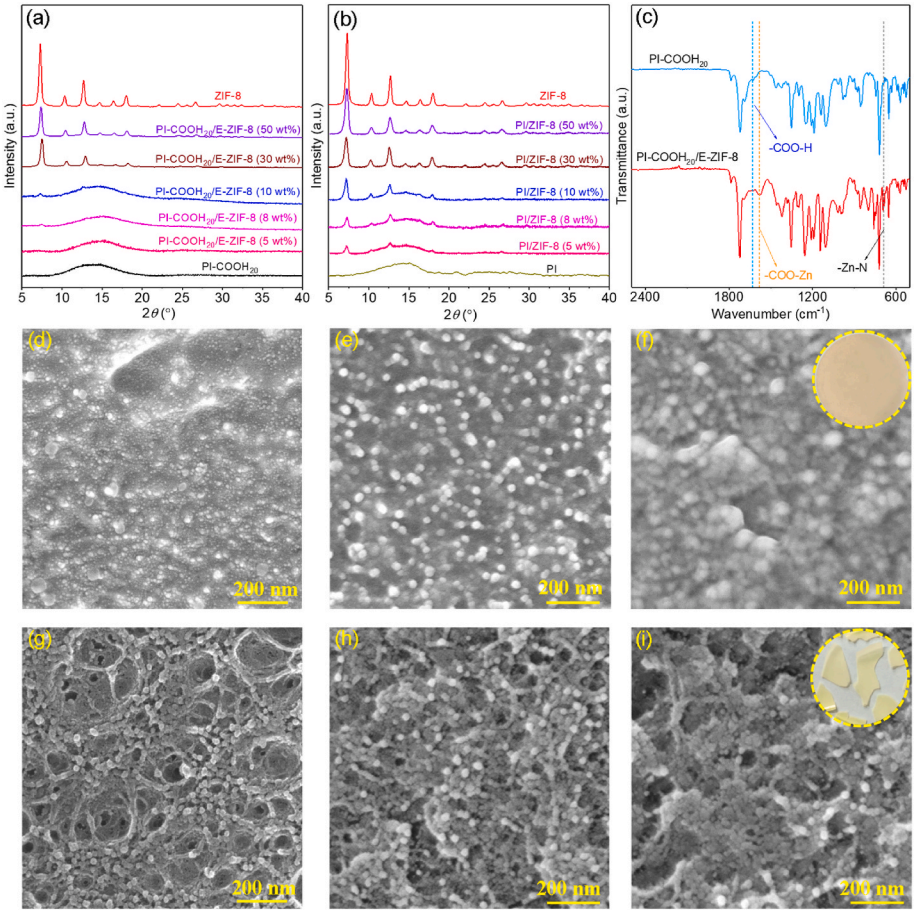

Fig. 3. (a) WAXD patterns of ZIF-8 nanoparticles and PI-$COOH_{20}$/E-ZIF-8 (5, 8, 10, 30, and 50 wt%) membranes. (b) WAXD patterns of ZIF-8 nanoparticles and PI/ZIF-8 (5, 8, 10, 30, and 50 wt%) membranes. (c) ATR-FTIR spectra of PI-$COOH_{20}$ and PI-$COOH_{20}$/E-ZIF-8 (40 wt%) membranes. Cross-sectional SEM images of (d) PI-$COOH_{20}$/E-ZIF-8 (10 wt%), (e) PI-$COOH_{20}$/E-ZIF-8 (40 wt%), (f) PI-$COOH_{20}$/E-ZIF-8 (50 wt%), (g) PI/ZIF-8 (10 wt%), (h) PI/ZIF-8 (40 wt%), and (i) PI/ZIF-8 (50 wt%) membranes. Inset: Optical images of (f) PI-$COOH_{20}$/E-ZIF-8 (50 wt%) and (i) PI/ZIF-8 (50 wt%) membranes.

1s, and F 1s signals of PI-$COOH_{20}$ membrane, the Zn 2p signal was detected in PI-$COOH_{20}$/E-ZIF-8 membranes, indicating the successful mixing of ZIF-8 with PI-$COOH_{20}$. Fig. S7 shows the high-resolution O 1s spectra of PI-$COOH_{20}$ and PI-$COOH_{20}$/E-ZIF-8 (40 wt%) membranes. In the spectrum of PI-$COOH_{20}$ membrane, the fitted peaks at 532.1 and 532.8 eV belongs to C═O and –COO–, respectively. However, the peak at 532.8 eV shifts to 533.2 eV in the spectrum of PI-$COOH_{20}$/E-ZIF-8 (40 wt%) membrane, suggesting the formation of –COO–Zn^{2+} coordination bond.

Molecular simulation was performed to study the *in-situ* etching ZIF-8 in PI-$COOH_{20}$ matrix in molecular level (Fig. 4). The obtained ZIF-8 nanoparticles have rhombic dodecahedral shape and thus the (110) slab of ZIF-8 is the dominantly present facet. Meanwhile, the surface energy of (100) is only 0.07 J m^{-2} higher than (110). Thus, both (110) and (100) of ZIF-8 were considered to perform the simulation. The substitution energy for substituting an imidazole group by a carboxyl group of PI-$COOH_{20}$ polyimide was calculated by the following equation (1):

$$E_{sub} = E_{ZIF-8\ slab-Hmin+PI} + E_{Hmin} - E_{ZIF-8\ slab} - E_{PI} \quad (2)$$

where the $E_{ZIF\text{-}8\ slab\text{-}Hmin\ +\ PI}$ is the energy of ZIF-8, which the slab of one imidazole linker substituted by PI-$COOH_{20}$, $E_{ZIF\text{-}8}$ is the energy of the (100) or (110) slab of ZIF-8, E_{PI} and.

E_{Hmin} is the energy of PI-$COOH_{20}$ and the neutral imidazole linker in the gas phase, respectively. The energy of substituting imidazole by PI-$COOH_{20}$ on (100) and (110) slabs of ZIF-8 are −2.28 eV and −4.53 eV, respectively. Both substitution processes are exothermic and therefore feasible. The molecular simulation results prove that the carboxyl group of PI-$COOH_{20}$ can substitute 2-methylimidazole ligands of ZIF-8 nanoparticles and form coordination bonds with exposed Zn^{2+} sites.

3.3. Gas separation performance of PI-$COOH_x$/E-ZIF-8 membranes

PI and PI-$COOH_x$ (x = 20, 30, 50) polyimides with 0%, 20%, 30%, and 50% carboxyl group (molar ratio of DABA) were synthesized to study the effects of carboxyl content on gas separation performance of hybrid membranes. The chemical formulas of these polyimides are shown in Fig. 5a. ZIF-8 loading is fixed at 40 wt% for all the hybrid membranes. The pure gas permeation properties of pristine polymer membranes and hybrid membranes were measured using a fixed-volume pressure increase time-lag apparatus with 3 bar feed gas at 35 °C. Tables S1 and S2 summarize and compare the gas permeability and selectivity of these membranes. The gas permeability of PI-$COOH_x$/E-ZIF-8 (40 wt%) membranes follows the order of kinetic diameter: H_2 (2.89 Å) > CO_2 (3.3 Å) > O_2 (3.46 Å) > N_2 (3.6 Å) > CH_4 (3.8 Å), showing obvious molecular sieving effect. Comparing with their pristine PI-$COOH_x$ membranes, the H_2 permeability enhancement ratio of PI/ZIF-8 (40 wt%), PI-$COOH_{20}$/E-ZIF-8 (40 wt%), PI-$COOH_{30}$/E-ZIF-8 (40 wt%), and PI-$COOH_{50}$/E-ZIF-8 (40 wt%) membranes is 792.3%, 241.6%, 180.5% and 5.8%, respectively (Fig. 5b). WAXD patterns had been tested to study the structure of those hybrid membranes (Fig. S8). All of them were well matched with ZIF-8 patterns, confirming the existence of ZIF-8 crystals in all the membranes. These existed ZIF-8 crystals provide gas channels to contribute to the permeability enhancement. With the carboxyl content increases from 0% to 50%, the gas permeability enhancement ratio of PI-$COOH_x$/E-ZIF-8 (40 wt%) membranes gradually decreases. This may because the increased carboxyl could etch ZIF-8 more deeply, leaving less gas permeation channels from ZIF-8 crystals. Notably, although ZIF-8 structure still can be seen in hybrid membrane, the gas permeability of PI-$COOH_{50}$/E-ZIF-8 (40 wt%) membrane is similar or even lower than that of PI-$COOH_{50}$ membrane. It is reasonable to infer that the pore blockage caused by

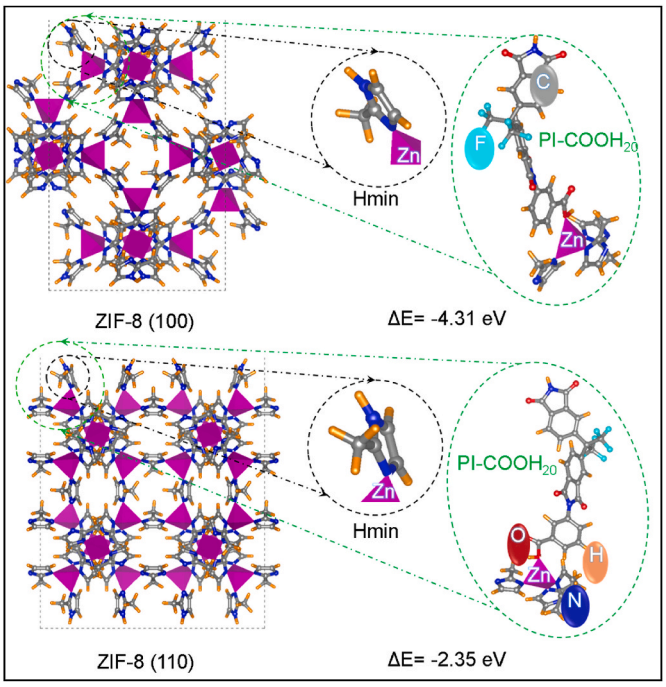

Fig. 4. Molecular simulation of PI-$COOH_{20}$ polyimide (one repeat unit) coordinated on the unsaturated metal sites of (100) and (110) slabs of ZIF-8 after removing a 2-methylimidazole (Hmin) linker. The substitution energy of a 2-methylimidazole linker (ΔE) by PI-$COOH_{20}$ polyimide (one repeat unit) is noted on the side. Colors codes: C, grey; N, blue; H, orange; Zn, violet. (For interpretation of the references to colour in this figure legend, the reader is referred to the Web version of this article.)

excess coordination bonds between ZIF-8 and PI-$COOH_{50}$ hinders increase of gas permeability.

The ideal selectivity of PI-$COOH_x$/E-ZIF-8 (40 wt%) hybrid membranes are obviously improved in comparison of pristine polymer membranes. Compared with the pristine PI-$COOH_x$ membranes, the H_2/CH_4 selectivity variation ratio of PI/ZIF-8 (40 wt%), PI-$COOH_{20}$/E-ZIF-8 (40 wt%), PI-$COOH_{30}$/E-ZIF-8 (40 wt%) and PI-$COOH_{50}$/E-ZIF-8 (40 wt %) membranes is −29.9%, 59%, 63.8%, and 176.2%, respectively. Obviously, the ideal selectivity of PI/ZIF-8 (40 wt%) membrane is even lower than that of PI membrane, which is mainly attributed to the weak interfacial interaction between PI matrix and ZIF-8 fillers. In contrast, the ideal selectivity of hybrid membrane with carboxyl polyimide matrix is all improved. With the carboxyl content increase, the selectivity enhancement ratio gradually increases. This is probably because the interchain distance of polyimides is gradually tightened by the formation of much more coordination bonds. The simultaneous enhancement of gas permeability and selectivity for PI-$COOH_x$/E-ZIF-8 (40 wt%) confirms the significant role of carboxyl groups in ZIF-8 hybrid membranes. However, too many carboxyl groups would result in low permeability and too few carboxyl groups would lead to low selectivity. Based on above discussion, the PI-$COOH_{20}$ polyimide was selected as matrix for subsequent research.

The different ZIF-8 loading (5, 10, 20, 30, 40, and 50 wt%) effect on gas separation performance of hybrid membranes was further studied. The gas permeability and selectivity of PI-$COOH_{20}$ and PI-$COOH_{20}$/E-ZIF-8 membranes are shown and summarized (Fig. S9 and Table S3). The H_2, CO_2, O_2, N_2, and CH_4 permeability of pristine PI-$COOH_{20}$ membrane is 538.0, 368.0, 102.4, 26.2, and 23.0 Barrer, respectively. After the addition of 5 wt% ZIF-8, the hybrid membrane shows reduction in gas permeability and increase in ideal selectivity. This is because almost all the ZIF-8 nanoparticles decompose after reacting with excess carboxyl groups, and the coordination bond between Zn^{2+} and PI-$COOH_{20}$ tightens the interchain distance and thus hinders the diffusion of gases. With the ZIF-8 loading further increases to 50 wt%, the H_2, CO_2, O_2, N_2, and CH_4 permeability of PI-$COOH_{20}$/E-ZIF-8 (50 wt%) raise to 3058.6, 1429.0, 459.0, 99.6, and 81.4 Barrer, increasing by 468.5%, 288.3%, 348.2%, 280.1%, 253.9%, respectively. The increasing ratio of gas permeability for small-sized gases (H_2, O_2 and CO_2) is larger than large-sized gases (N_2 and CH_4), which can be attributed to the internal channels of ZIF-8 that promotes fast transport of small-sized gases.

As a result, the gas selectivity for H_2/N_2, H_2/CH_4, O_2/N_2, and CO_2/CH_4 gas pairs are greatly improved from 20.3, 23.4, 3.9 and 16.0 of pristine PI-$COOH_{20}$ membrane to 30.7, 37.6, 4.6 and 17.6 of PI-$COOH_{20}$/E-ZIF-8 (50 wt%) membrane (Fig. S9). For H_2/N_2, H_2/CH_4, and O_2/N_2 gas pairs, the gas permeability and selectivity of PI-$COOH_{20}$/E-ZIF-8 membranes show simultaneous enhancement with the increasing ZIF-8 loading.

The comprehensive gas separation performance of PI-$COOH_{20}$/E-ZIF-8 membranes for H_2/N_2, H_2/CH_4, O_2/N_2, and CO_2/CH_4 gas pairs are summarized in the upper bound plots, as shown in Fig. 5c, 5d, 5e and 5f. H_2 and O_2 permeability and H_2/N_2, H_2/CH_4, and O_2/N_2 selectivity of PI-$COOH_{20}$/E-ZIF-8 membranes increase simultaneously with the increasing ZIF-8 loading, surpassing the 2008 upper bound and approaching the 2015 upper bound gradually [53,54]. However, the CO_2/CH_4 selectivity of PI-$COOH_{20}$/E-ZIF-8 membrane reaches the maximum value at the ZIF-8 loading of 5 wt% and then decreases with the increase of ZIF-8 loading. At lower ZIF-8 loading, more Zn ions are exposed on etched ZIF-8 surfaces. These Zn ions are prone to interact with CO_2, which enables favorable CO_2 solubility selectivity and the improvement of CO_2/CH_4 permeability selectivity. At higher ZIF-8 loading, less Zn ions are exposed on etched ZIF-8 surfaces due to inadequate carboxylic acid groups, which cause the decrease of CO_2/CH_4 solubility selectivity. The gas separation performance of PI/ZIF-8 (40 wt %) membranes is also plotted for comparison. Although the PI/ZIF-8 (40 wt%) membrane exhibits high gas permeability (7574.2 Barrer for H_2, 5581.9 Barrer for CO_2 and 2573.4 Barrer for O_2), but ideal selectivity (9.2, 10.1, 3.1, 7.4 for H_2/N_2, H_2/CH_4, O_2/N_2 and CO_2/CH_4, respectively) are much lower than those of PI membranes and PI-$COOH_{20}$/E-ZIF-8 membranes, which is due to the formation of rich interfacial defects between PI and ZIF-8. This also verifies the significance of the *in-situ* etching ZIF-8 strategy for preparing high-performance hybrid membranes.

Gas adsorption tests were performed to understand the gas transport mechanism of PI-$COOH_{20}$/E-ZIF-8 membranes. Fig. S10 shows the H_2, CO_2, and CH_4 adsorption isotherms of PI-$COOH_{20}$ and PI-$COOH_{20}$/E-ZIF-8 membranes, and Brunauer-Emmett-Teller (BET) surface area and gas adsorption capacity are summarized in Table S4. The BET surface area of PI-$COOH_{20}$/E-ZIF-8 (10 wt%) membrane is 241.3 m^2/g, which is almost the same with that of pristine PI-$COOH_{20}$ membrane (249.9 m^2/g). With the ZIF-8 loading increasing to 30 and 50 wt%, the B.E.T surface area of PI-$COOH_{20}$/E-ZIF-8 (30 wt%) and PI-$COOH_{20}$/E-ZIF-8 (50 wt%) membrane largely increases to 358.6 and 550.8 m^2/g, respectively. At the same time, CO_2 and CH_4 adsorption capacity increases from 29.6 and 5.5 cm^3/g of PI-$COOH_{20}$/E-ZIF-8 (10 wt%) membrane to 31.3 and 8.0 cm^3/g of PI-$COOH_{20}$/E-ZIF-8 (50 wt%) membrane. The increased B.E.T surface area and adsorption capacity can be attributed to the introduction of microporous ZIF-8 nanoparticles. As calculated from gas adsorption data and permeation data, the solubility coefficient (S), diffusion coefficient (D) of H_2, CH_4 and CO_2, the relative solubility selectivity (α_D) and diffusion selectivity (α_S) are summarized and illustrated (Fig. 6a–d). With the ZIF-8 loading increasing from 0 wt% to 50 wt%, the H_2 diffusion coefficient increases from 1022.2×10^{-8} cm^2/s to 5405.9×10^{-8} cm^2/s, the CO_2 diffusion coefficient increase from 8.8×10^{-8} cm^2/s to 34.7×10^{-8} cm^2/s, and the CH_4 diffusion coefficient increases from 2.6×10^{-8} cm^2/s to 7.7×10^{-8} cm^2/s, which increases by 428.8%, 294.3%, and 196.2%, respectively. The increasing ratio follows the order of kinetic diameter: H_2 (2.89 Å) > CO_2 (3.3 Å) > CH_4 (3.8 Å), indicating the diffusion selectivity are greatly enhanced from 397.6 and 116.6 of pristine PI-$COOH_{20}$ membrane to 699.1 and 155.8 of

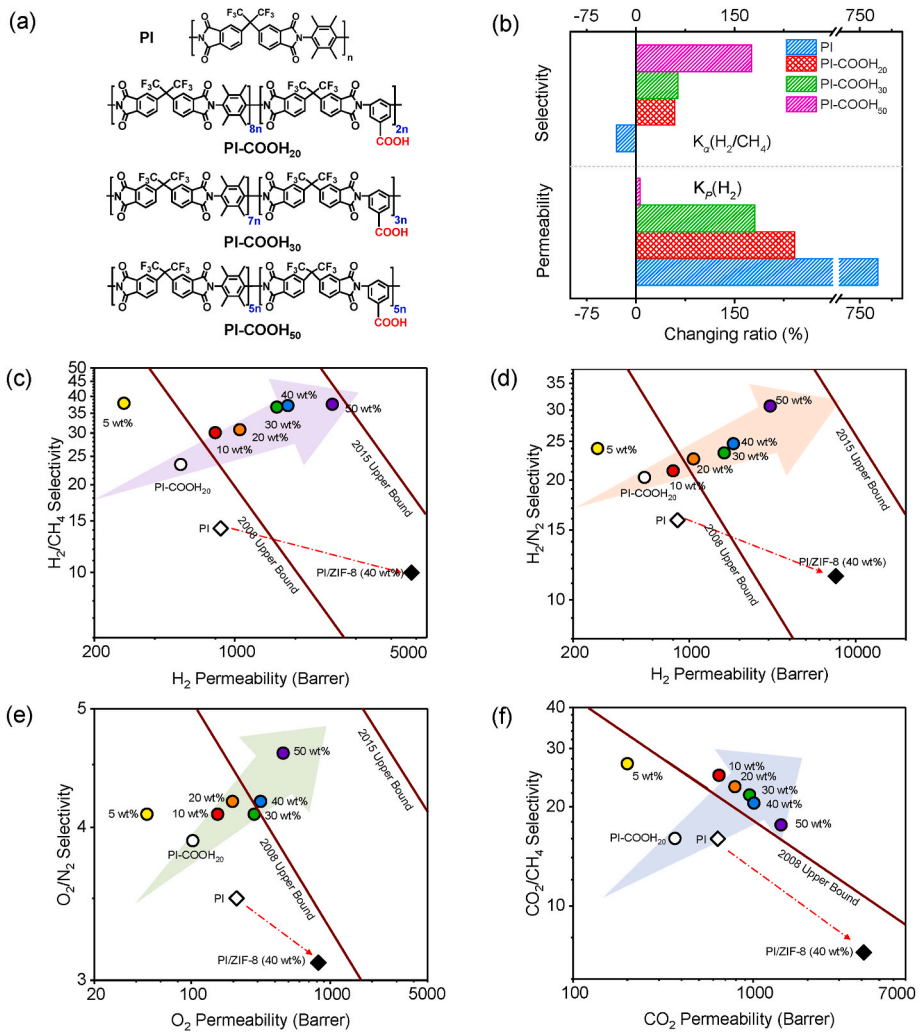

Fig. 5. (a) Chemical structures of PI, PI-COOH$_{20}$, PI-COOH$_{30}$, and PI-COOH$_{50}$ polyimides. (b) Enhancement percentage of H_2 permeability and H_2/CH_4 selectivity of PI/ZIF-8 (40 wt%), PI-COOH$_{20}$/E-ZIF-8 (40 wt%), PI-COOH$_{30}$/E-ZIF-8 (40 wt%), and PI-COOH$_{50}$/E-ZIF-8 (40 wt%) membranes compared with corresponding pristine polymer membrane. Relationships between gas permeability and gas pair selectivity of PI, PI-COOH$_{20}$, PI/ZIF-8 (40 wt%) and PI-COOH$_{20}$/E-ZIF-8 (5, 10, 20, 30, 40 and 50 wt%) membranes with 2008 and 2015 upper bound for (c) H_2/N_2, (d) H_2/CH_4, (e) O_2/N_2, and (f) CO_2/CH_4 gas pairs.

PI-COOH$_{20}$/E-ZIF-8 (50 wt%) membrane, which increases by 75.8% and 33.6%, respectively. It is probably because the rich microspores and regular channels inside ZIF-8 nanoparticles promote selective diffusion of small gases like H_2. The H_2/CH_4 and H_2/CO_2 solubility selectivity slightly change from 0.06 and 0.01 of pristine PI-COOH$_{20}$ membrane to 0.05 and 0.01 of PI-COOH$_{20}$/E-ZIF-8 (50 wt%) membrane, showing negligible effects of ZIF-8 incorporation on solubility selectivity.

When polymer membranes are exposed to high-pressure condensable gases such as CO_2, plasticization usually occurs, which results in gas permeability increase and serious loss of selectivity [55]. CO_2 permeability of PI-COOH$_{20}$ and PI-COOH$_{20}$/E-ZIF-8 membranes as a function of *trans*-membrane pressure was tested to evaluate the plasticization resistance of prepared hybrid membranes. As shown in Fig. 6e, the pristine PI-COOH$_{20}$ membrane plasticizes rapidly at 6 bar. However, PI-COOH$_{20}$/E− ZIF-8 (30 wt%) membrane shows no sign of plasticization until the pressure increases to 27 bar. The plasticization pressure of PI-COOH$_{20}$/E-ZIF-8 (30 wt%) membrane shows 350% increase compared with that of pristine PI-COOH$_{20}$ membrane, which can be attributed to the limited chain mobility of polyimide by the strong coordination bond between ZIF-8 and PI-COOH$_{20}$. An equimolar CO_2/CH_4 gas mixture (50:50) was further used to evaluate the stability of PI-COOH$_{20}$/E-ZIF-8 membranes. The CO_2/CH_4 selectivity as a function of feed gas pressure is illustrated in Fig. 6f. The CO_2/CH_4 selectivity of pristine PI-COOH$_{20}$ membrane decreases from 17.3 to 13.6 with the feed gas pressure increasing from 3 bar to 15 bar, showing a 21.4% decrease. In contrast, the CO_2/CH_4 selectivity of PI-COOH$_{20}$/E-ZIF-8 (30 wt%) membrane slightly increases from 20.2 to 22.4, increasing by 10.9%. These results demonstrate the improved separation stability of hybrid membranes with *in-situ* etched ZIF-8 even under high-pressure mixed gas, showing the great prospect for practical application.

4. Conclusion

In this work, surface etching of ZIF-8 nanoparticles was engineered to enhance the interfacial interaction of hybrid membranes. The decomposition phenomenon of ZIF-8 nanoparticles in acid condition was first studied in detail. The 2-methylimidazole ligands on outer surface of ZIF-8 can be substituted by acid molecules without damaging the cage structure. Based on this mechanism, ZIF-8 nanoparticles were incorporated into carboxyl-contained polyimide and *in-situ* etched by acid groups. The coordination bonds strongly enhance the interfacial interaction between ZIF-8 nanoparticles and PI-COOH$_{20}$ matrix, and thus effectively eliminate interfacial defects in hybrid membranes. In comparison with pristine PI-COOH$_{20}$ membrane, PI-COOH$_{20}$/E-ZIF-8 hybrid membranes show simultaneously improved gas permeability and selectivity, surpassing the 2008 upper bound and approaching the 2015 upper bound for H_2/N_2, H_2/CH_4, O_2/N_2, and CO_2/CH_4 gas pairs. Moreover, PI-COOH$_{20}$/E-ZIF-8 (30 wt%) hybrid membrane exhibits excellent anti-plasticization properties with a 350% increase in the plasticization pressure (6 bar vs 27 bar), and shows highly stable CO_2/CH_4 selectivity under mixed gas. This work provides a new strategy of *in-situ* etching ZIF-8 for effectively eliminating interfacial defects and

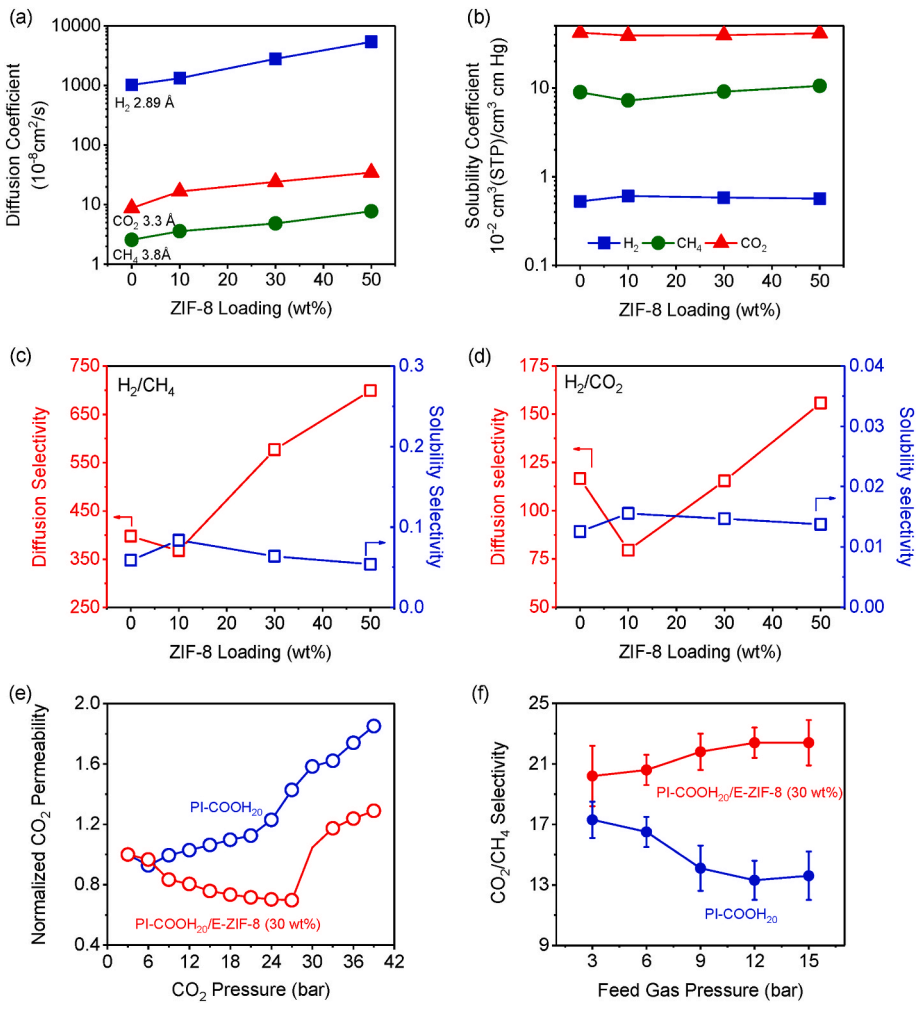

Fig. 6. H_2, CO_2 and CH_4 diffusion coefficients (a) and solubility coefficients (b) of PI-COOH$_{20}$ and PI-COOH$_{20}$/E-ZIF-8 (10, 30, and 50 wt%) membranes. (c) H_2/CH_4 diffusion selectivity and solubility selectivity and (d) H_2/CO_2 diffusion selectivity and solubility selectivity of PI-COOH$_{20}$ and PI-COOH$_{20}$/E-ZIF-8 (10, 30, and 50 wt%) membranes. (e) Variation trends of the normalized CO_2 permeability of PI-COOH$_{20}$ and PI-COOH$_{20}$/E-ZIF-8 (30 wt%) membranes with increasing pure gas pressure. (f) Variation trends of CO_2/CH_4 selectivity of PI-COOH$_{20}$ and PI-COOH$_{20}$/E-ZIF-8 (30 wt%) membranes with increasing mixed gas pressure.

breaking the trade-off limit on gas separation performance of hybrid membranes.

Author contributions

Zhenggong Wang and Jian Jin designed the experiments. Huiyuan Jiao and Yanshu Shi conducted the experiments and material characterizations. Kuan Lu conducted the molecular simulations. Yapeng Shi, Feng Zhang and Yatao Zhang provided helpful discussion. Huiyuan Jiao, Yanshu Shi, Zhenggong Wang and Jian Jin wrote the manuscript. All of the authors participated in the discussion and read the manuscript.

Declaration of competing interest

The authors declare that they have no known competing financial interests or personal relationships that could have appeared to influence the work reported in this paper.

Data availability

No data was used for the research described in the article.

Acknowledgment

This work was supported by the National Natural Science Foundation of China (21988102, 51873230, 51803145). We would like to thank the support from Jiangsu Key Laboratory of Advanced Functional Polymer Design and Application, Soochow University.

Appendix A. Supplementary data

Supplementary data to this article can be found online at https://doi.org/10.1016/j.memsci.2022.121146.

References

[1] T.S. Chung, L.Y. Jiang, Y. Li, S. Kulprathipanja, Mixed matrix membranes (MMMs) comprising organic polymers with dispersed inorganic fillers for gas separation, Prog. Polym. Sci. 32 (2007) 483–507, https://doi.org/10.1016/j.progpolymsci.2007.01.008.
[2] N.W. Ockwig, T.M. Nenoff, Membranes for hydrogen separation, Chem. Rev. 110 (2010) 2573–2574, https://doi.org/10.1021/cr0501792.
[3] R.M. Tieado, N. Yuriychuk, M. Iglesias, M.L. Gonzalez, E.M. Maya, Mixed matrix membranes containing a biphenyl-based knitting aryl polymer and gas separation performance, Membranes 11 (2021), 11120914, https://doi.org/10.3390/membranes11120914.
[4] Q. Qian, P.A. Asinger, M.J. Lee, G. Han, K.M. Rodriguez, S. Lin, F.M. Benedetti, A. X. Wu, W.S. Chi, Z.P. Smith, MOF-based membranes for gas separations, Chem. Rev. 120 (2020) 8161–8266, https://doi.org/10.1021/acs.chemrev.0c00119.
[5] N. Kosinov, J. Gascon, F. Kapteijn, E.J.M. Hensen, Recent developments in zeolite membranes for gas separation, J. Membr. Sci. 499 (2016) 65–79, https://doi.org/10.1016/j.memsci.2015.10.049.
[6] Y.S. Li, F.Y. Liang, H. Bux, A.F. Ff, W.S. Yang, J. Caro, Molecular sieve membrane: supported metal-organic framework with high hydrogen selectivity, Angew. Chem. Int. Ed. 122 (2010) 558–561, https://doi.org/10.1002/ange.200905645.
[7] M. Rungta, G.B. Wenz, C. Zhang, L. Xu, W. Qiu, J.S. Adams, W.J. Koros, Carbon molecular sieve structure development and membrane performance relationships, Carbon 115 (2017) 237–248, https://doi.org/10.1016/j.carbon.2017.01.015.
[8] K. Hazazi, X. Ma, Y. Wang, W. Ogieglo, A. Alhazmi, Y. Han, I. Pinnau, Ultra-selective carbon molecular sieve membranes for natural gas separations based on a

carbon-rich intrinsically microporous polyimide precursor, J. Membr. Sci. 585 (2019) 1–9, https://doi.org/10.1016/j.memsci.2019.05.020.
[9] L.Q. Hu, V.T. Bul, A. Krishnamurthy, S.H. Fan, W. Guo, S. Pal, X.Y. Chen, G. Y. Zhang, Y.F. Ding, R.P. Singh, M. Luplon, H.Q. Lin, Tailoring sub-3.3 Å ultramicropores in advanced carbon molecular sieve membranes for blue hydrogen production, Sci. Adv. 8 (2022), 18160, https://doi.org/10.1126/sciadv.abl8160.
[10] O. Shekhah, J. Liu, R.A. Fischer, C. Woll, MOF thin films: existing and future applications, Chem. Soc. Rev. 40 (2011) 1081–1106, https://doi.org/10.1002/chin.201125263.
[11] M. Askari, T.S. Chung, Natural gas purification and olefin/paraffin separation using thermal cross-linkable co-polyimide/ZIF-8 mixed matrix membranes, J. Membr. Sci. 444 (2013) 173–183, https://doi.org/10.1016/j.memsci.2013.05.016.
[12] S.W. Zhu, X.Y. Bi, Y.P. Shi, Y.S. Shi, Y.T. Zhang, J. Jin, Z.G. Wang, Thin films based on polyimide/metal-organic framework nanoparticle composite membranes with substantially improved stability for CO_2/CH_4 separation, ACS Appl. Nano Mater. 5 (2022) 8997–9007, https://doi.org/10.1021/acsanm.2c01248.
[13] Z.G. Wang, H.T. Ren, S.X. Zhang, F. Zhang, J. Jin, Polymers of intrinsic microporosity/metal-organic framework hybrid membranes with improved interfacial interaction for high-performance CO_2 separation, J. Mater. Chem. 5 (2017) 10968–10977, https://doi.org/10.1039/c7ta01773a.
[14] Y. Bai, Y. Dou, L.H. Xie, W. Rutledge, J.R. Li, H.C. Zhou, Zr-based metal-organic frameworks: design, synthesis, structure, and applications, Chem. Soc. Rev. 45 (2016) 2327–2367, https://doi.org/10.1039/c5cs00837a.
[15] J.E. Bachman, Z.P. Smith, T. Li, T. Xu, J.R. Long, Enhanced ethylene separation and plasticization resistance in polymer membranes incorporating metal-organic framework nanocrystals, Nat. Mater. 15 (2016) 845–849, https://doi.org/10.1038/nmat4621.
[16] Z. Wang, Y. Tian, W. Fang, B.B. Shrestha, M. Huang, J. Jin, Constructing strong interfacial interactions under mild conditions in MOF-incorporated mixed matrix membranes for gas separation, ACS Appl. Mater. Interfaces 13 (2021) 3166–3174, https://doi.org/10.1021/acsami.0c19554.
[17] X.Y. Bi, Y.A. Zhang, F. Zhang, S.X. Zhang, Z.G. Wang, J. Jin, MOF nanosheet-based mixed matrix membranes with metal-organic coordination interfacial interaction for gas separation, ACS Appl. Mater. Interfaces 12 (2020) 49101–49110, https://doi.org/10.1021/acsami.0c14639.
[18] Y.P. Shi, Z.G. Wang, Y.S. Shi, S.W. Zhu, K. Lu, Y.T. Zhang, J. Jin, Micrometer-sized MOF particles incorporated mixed-matrix membranes driven by π-π interfacial interactions for improved gas separation, Separ. Purif. Technol. 295 (2022), 121258, https://doi.org/10.1016/j.seppur.2022.121258.
[19] P. Burmann, B. Zornoza, C. Téllez, J. Coronas, Mixed matrix membranes comprising MOFs and porous silicate fillers prepared *via* spin coating for gas separation, Chem. Eng. Sci. 107 (2014) 66–75, https://doi.org/10.1016/j.ces.2013.12.001.
[20] X.Y. Chen, H.V. Thang, D. Rodrigue, S. Kaliaguine, Effect of macrovoids in nano-silica/polyimide mixed matrix membranes for high flux CO_2/CH_4 gas separation, RSC Adv. 4 (2014) 12235–12244, https://doi.org/10.1039/c3ra47208f.
[21] T.T. Moore, W.J. Koros, Non-ideal effects in organic-inorganic materials for gas separation membranes, J. Mol. Struct. 739 (2005) 87–98, https://doi.org/10.1016/j.molstruc.2004.05.043.
[22] B. Zornoza, A.M. Joaristi, P.S. Crespo, C. Tellez, J. Coronas, J. Gascon, F. Kapteijn, Functionalized flexible MOFs as fillers in mixed matrix membranes for highly selective separation of CO_2 from CH_4 at elevated pressures, Chem. Commun. 47 (2011) 9522–9524, https://doi.org/10.1039/C1CC13431K.
[23] M.W. Anjum, F. Vermoortele, A.L. Khan, B. Bueken, D. Vos, I. Vankelecom, Modulated UiO-66-based mixed-matrix membranes for CO_2 separation, ACS Appl. Mater. Interfaces 7 (2015) 25193–25201, https://doi.org/10.1021/acsami.5b08964.
[24] G. Liu, K. Huang, Q. Li, K. Guan, Y. Li, W. Jin, UiO-66-polyether block amide mixed matrix membranes for CO_2 separation, J. Membr. Sci. 513 (2016) 155–165, https://doi.org/10.1016/j.memsci.2016.04.045.
[25] Y. Jiang, C. Liu, C. Jürgen, A. Huang, A new UiO-66-NH_2 based mixed-matrix membranes with high CO_2/CH_4 separation performance, Microporous Mesoporous Mater. 274 (2018) 203–211, https://doi.org/10.1016/j.micromeso.2018.08.003.
[26] Z. Tahir, M. Aslam, M.A. Gilani, M.R. Bilad, M.W. Anjum, L.P. Zhu, A.L. Khan, SO_3H functionalized UiO-66 nanocrystals in polysulfone based mixed matrix membranes: synthesis and application for efficient CO_2 capture, Separ. Purif. Technol. 224 (2019) 524–533, https://doi.org/10.1016/j.seppur.2019.05.060.
[27] D.H. Hong, M.P. Suh, Enhancing CO_2 separation ability of a metal-organic framework by post-synthetic ligand exchange with flexible aliphatic carboxylates, Chemistry 20 (2014) 426–434, https://doi.org/10.1002/chem.201303801.
[28] N. Zhang, B.L. Wang, Y.R. Zhang, F.Z. Bu, C. Ying, X.F. Li, C.J. Zhao, H. Na, Mechanically reinforced phosphoric acid doped quaternized poly(ether ether ketone) membranes *via* cross-linking with functionalized graphene oxide, Chem. Commun. 50 (2014) 15381–15384, https://doi.org/10.1039/C4CC07791A.
[29] J. Zhao, Y.W. Zhu, G.W. He, R.S. Xing, F.S. Pan, Z.Y. Jiang, P. Zhang, X.Z. Cao, B. Y. Wang, Incorporating zwitterionic graphene oxides into sodium alginate membrane for efficient water/alcohol separation, ACS Appl. Mater. Interfaces 8 (2016) 2097–2103, https://doi.org/10.1021/acsami.5b10551.
[30] H.L. Wang, S.F. He, X.D. Qin, C.E. Li, T. Li, Interfacial engineering in metal-organic framework-based mixed matrix membranes using covalently grafted polyimide brushes, J. Am. Chem. Soc. 140 (2018) 17203–17210, https://doi.org/10.1021/jacs.8b10138.
[31] Z.G. Wang, D. Wang, S.X. Zhang, L. Hu, J. Jin, Interfacial design of mixed matrix membranes for improved gas separation performance, Adv. Mater. 28 (2016) 3399–3405, https://doi.org/10.1002/adma.201504982.
[32] V. Nafisi, M.B. Hägg, Gas separation properties of ZIF-8/6FDA-Durene diamine mixed matrix membrane, Separ. Purif. Technol. 128 (2014) 31–38, https://doi.org/10.1016/j.seppur.2014.03.006.
[33] Y. Peng, Y.S. Li, Y.J. Ban, W.S. Yang, Two-dimensional metal-organic framework nanosheets for membrane-based gas separation, Angew. Chem., Int. Ed. 56 (2017) 9757–9761, https://doi.org/10.1002/anie.201703959.
[34] S. Kim, E. Shamsaei, X. Lin, Y. Hu, G.P. Simon, J.G. Seong, J.S. Kim, W.H. Lee, Y. M. Lee, H. Wang, The enhanced hydrogen separation performance of mixed matrix membranes by incorporation of two-dimensional ZIF-L into polyimide containing hydroxyl group, J. Membr. Sci. 549 (2018) 260–266, https://doi.org/10.1016/j.memsci.2017.12.022.
[35] S. Feng, M. Bu, J. Pang, W. Fan, D. Sun, Hydrothermal stable ZIF-67 nanosheets *via* morphology regulation strategy to construct mixed-matrix membrane for gas separation, J. Membr. Sci. 593 (2019), 117404, https://doi.org/10.1016/j.memsci.2019.117404.
[36] M.H. Huang, Z.G. Wang, J. Jin, Two-dimensional microporous material-based mixed matrix membranes for gas separation, Chem. Asian J. 15 (2020) 2303–2315, https://doi.org/10.1002/asia.202000053.
[37] L. Feng, K.Y. Wang, G.S. Day, M.R. Ryder, H.C. Zhou, Destruction of metal-organic frameworks: positive and negative aspects of stability and lability, Chem. Rev. 120 (2020) 13087–13133, https://doi.org/10.1021/acs.chemrev.0c00722.
[38] Z. Fang, B. Bueken, D.E.D. Vos, R.A. Fischer, Defect-engineered metal-organic frameworks, Angew. Chem. Int. Ed. 54 (2015) 7234–7254, https://doi.org/10.1002/anie.201411540.
[39] H.F. Li, P. Wu, Y.W. Xiao, M. Shao, Y. Shen, Y. Fan, H.H. Chen, R.J. Xie, W. L. Zhang, S. Li, J.S. Wu, Y. Fu, B. Zheng, W.N. Zhang, F.W. Huo, Metal-organic frameworks as metal ion precursors for the synthesis of nanocomposites for lithium-ion batteries, Angew. Chem. Int. Ed. 59 (2020) 4763–4769, https://doi.org/10.1002/anie.201915279.
[40] R. Du, Y.F. Wu, Y.C. Yang, T. Zhai, T.T. Zhou, Q.Y. Shang, L.H. Zhu, C.X. Shang, Z. X. Guo, Porosity engineering of MOF-based materials for electrochemical energy storage, Adv. Energy Mater. 11 (2021), 2100154, https://doi.org/10.1002/aenm.202100154.
[41] Y.C. Zhou, M.M. Jia, X.F. Zhang, J.F. Yao, Etched ZIF-8 as a filler in mixed-matrix membranes for enhanced CO_2/N_2 separation, Chem. Eur J. 26 (2020) 7918–7922, https://doi.org/10.1002/chem.202000965.
[42] T.H. Lee, J.G. Jung, Y.J. Kim, J.S. Roh, H.W. Yoon, B.S. Ghanem, H.W. Kim, Y. H. Cho, I. Pinnau, H.B. Park, Defect engineering in metal-organic frameworks towards advanced mixed matrix membranes for efficient propylene/propane separation, Angew. Chem. Int. Ed. 60 (2021) 13081–13088, https://doi.org/10.1002/anie.202100841.
[43] T.H. Lee, A. Ozcan, I. Park, D. Fan, J.K. Jang, P.G.M. Mileo, S.Y. Yoo, J.S. Roh, J. H. Kang, B.K. Lee, Y.H. Cho, R. Semino, H.W. Kim, G. Maurin, H.B. Park, Disclosing the role of defect-engineered metal-organic frameworks in mixed matrix membranes for efficient CO_2 separation: a joint experimental-computational exploration, Adv. Funct. Mater. 31 (2021), 2103973, https://doi.org/10.1002/adfm.202103973.
[44] S.H. Kunjattu, V. Ashok, A. Bhaskar, K. Pandare, R. Banerjee, U.K. Kharul, ZIF-8@DBzPBI-BUI composite membranes for olefin/paraffin separation, J. Membr. Sci. 549 (2018) 38–45, https://doi.org/10.1016/j.memsci.2017.11.069.
[45] J.S. Kim, S.J. Moon, H.H. Wang, S. Kim, Y.M. Lee, Mixed matrix membranes with a thermally rearranged polymer and ZIF-8 for hydrogen separation, J. Membr. Sci. 582 (2019) 381–390, https://doi.org/10.1016/j.memsci.2019.04.029.
[46] W.-H. Lai, G.L. Zhuang, H.-H. Tseng, M.-Y. Wey, Creation of tiny defects in ZIF-8 by thermal annealing to improve the CO_2/N_2 separation of mixed matrix membranes, J. Membr. Sci. 572 (2019) 410–418, https://doi.org/10.1016/j.memsci.2018.11.010.
[47] Z.G. Wang, A.P. Isfahani, K. Wakimoto, B.B. Shrestha, D. Yamaguchi, B. Ghalei, E. Sivaniah, Tuning the gas selectivity of Tröger's base polyimide membranes by using carboxylic acid and tertiary base interactions, ChemSusChem 11 (2018) 2744–2751, https://doi.org/10.1002/cssc.201801002.
[48] S.S. Wu, J.C. Liang, Y.P. Shi, M.H. Huang, X.Y. Bi, Z.G. Wang, J. Jin, Design of interchain hydrogen bond in polyimide membrane for improved gas selectivity and membrane stability, J. Membr. Sci. 618 (2021), 118659, https://doi.org/10.1016/j.memsci.2020.118659.
[49] X.F. Luo, Z.G. Wang, S.S. Wu, W.X. Fang, J. Jin, Metal ion cross-linked nanoporous polymeric membranes with improved organic solvent resistance for molecular separation, J. Membr. Sci. 621 (2021), 119002, https://doi.org/10.1016/j.memsci.2020.119002.
[50] J. Cravillon, S. Münzer, S.J. Lohmeier, A.F.K. Huber, Rapid room-temperature synthesis and characterization of nanocrystals of a prototypical zeolitic imidazolate framework, Chem. Mater. 21 (2009) 1410–1412. https://doi/10.1021/cm900166h.
[51] J.S. Laínez, B. Zornoza, S. Friebe, J. Caro, S. Cao, A. Sabetghadam, B. Seoane, J. Gascon, F. Kapteijn, C. Le Guillouzer, G. Clet, M. Daturi, C. Téllez, J. Coronas, Influence of ZIF-8 particle size in the performance of polybenzimidazole mixed matrix membranes for pre-combustion CO_2 capture and its validation through interlaboratory test, J. Membr. Sci. 515 (2016) 45–53, https://doi.org/10.1016/j.memsci.2016.05.039.
[52] J.S. Laínez, B. Zornoza, S. Friebe, J. Caro, S. Cao, A. Sabetghadam, B. Seoane, J. Gascon, F. Kapteijn, C. Le Guillouzer, G. Clet, M. Daturi, C. Téllez, J. Coronas, Influence of ZIF-8 particle size in the performance of polybenzimidazole mixed matrix membranes for pre-combustion CO_2 capture and its validation through interlaboratory test, J. Membr. Sci. 515 (2016) 45–53, https://doi.org/10.1016/j.memsci.2016.05.039.

[53] L.M. Robeson, The upper bound revisited, J. Membr. Sci. 320 (2008) 390–400, https://doi.org/10.1016/j.memsci.2008.04.030.
[54] L.M. Robeson, Q. Liu, B.D. Freeman, D.R. Paul, Comparison of transport properties of rubbery and glassy polymers and the relevance to the upper bound relationship, J. Membr. Sci. 476 (2015) 421–431, https://doi.org/10.1016/j.memsci.2014.11.058.
[55] J.H. Kim, W.J. Koros, D.R. Paul, Effects of CO_2 exposure and physical aging on the gas permeability of thin 6FDA-based polyimide membranespart 2. With crosslinking, J. Membr. Sci. 282 (2006) 32–43, https://doi.org/10.1016/j.memsci.2006.05.003.